AGU PUBLICATIONS

Geophysical Research Letters

RESEARCH LETTER
10.1002/2016GL072235

Key Points:
- We develop an *ET* partitioning method, by combining remote sensing, land surface model, and *LAI* regression obtained from in situ measurements
- We show that transpiration accounts for about 57.2% (with standard deviation ± 6.8%) of global terrestrial *ET*
- Uncertainty in canopy interception loss estimation is the largest source of bias in *ET* partitioning

Supporting Information:
- Supporting Information S1
- Figure S1
- Figure S2
- Figure S3
- Figure S4
- Figure S5
- Figure S6
- Figure S7
- Figure S8

Correspondence to:
Z. Wei,
Zhongwang.wei@yale.edu

Citation:
Wei, Z., K. Yoshimura, L. Wang, D. G. Miralles, S. Jasechko, and X. Lee (2017), Revisiting the contribution of transpiration to global terrestrial evapotranspiration, *Geophys. Res. Lett.*, *44*, 2792–2801, doi:10.1002/2016GL072235.

Received 4 DEC 2016
Accepted 15 MAR 2017
Accepted article online 20 MAR 2017
Published online 31 MAR 2017

Revisiting the contribution of transpiration to global terrestrial evapotranspiration

Zhongwang Wei[1], Kei Yoshimura[2,3], Lixin Wang[4], Diego G. Miralles[5,6], Scott Jasechko[7], and Xuhui Lee[1,8]

[1]School of Forestry and Environmental Studies, Yale University, New Haven, Connecticut, USA, [2]Institute of Industrial Science, University of Tokyo, Komaba, Tokyo, Japan, [3]Atmosphere and Ocean Research Institute, University of Tokyo, Kashiwa, Chiba, Japan, [4]Department of Earth Sciences, Indiana University-Purdue University Indianapolis, Indianapolis, Indiana, USA, [5]Department of Earth Sciences, VU University, Amsterdam, The Netherlands, [6]Laboratory of Hydrology and Water Management, Ghent University, Ghent, Belgium, [7]Department of Geography, University of Calgary, Calgary, Canada, [8]Yale-NUIST Center on Atmospheric Environment, Nanjing University of Information Science & Technology, Nanjing, Jiangsu, China

Abstract Even though knowing the contributions of transpiration (*T*), soil and open water evaporation (*E*), and interception (*I*) to terrestrial evapotranspiration ($ET = T + E + I$) is crucial for understanding the hydrological cycle and its connection to ecological processes, the fraction of *T* is unattainable by traditional measurement techniques over large scales. Previously reported global mean $T/(E + T + I)$ from multiple independent sources, including satellite-based estimations, reanalysis, land surface models, and isotopic measurements, varies substantially from 24% to 90%. Here we develop a new *ET* partitioning algorithm, which combines global evapotranspiration estimates and relationships between leaf area index (*LAI*) and $T/(E + T)$ for different vegetation types, to upscale a wide range of published site-scale measurements. We show that transpiration accounts for about 57.2% (with standard deviation ± 6.8%) of global terrestrial *ET*. Our approach bridges the scale gap between site measurements and global model simulations,and can be simply implemented into current global climate models to improve biological CO_2 flux simulations.

1. Introduction

Terrestrial evapotranspiration (*ET*) consists of evaporation from canopy-intercepted water (*I*), soil and open water evaporation (*E*), and transpiration (*T*) from plants. The contribution of *T* to *ET* ($T/(E + T + I)$) is a requirement for understanding changes in carbon assimilation and in water cycling in a changing environment and has received increasing attention from the scientific community in recent years [*Coenders-Gerrits et al.,* 2014; *Good et al.,* 2015; *Jasechko et al.,* 2013; *Maxwell and Condon*, 2016; *Miralles et al.,* 2016]. Although most of the published studies suggest that *T* accounts for the majority of the flux of vapor from terrestrial lands to the atmosphere, there remain significant uncertainties. As an example, *Miralles et al.* [2011] attributed about 80% of land *ET* to *T* based on a wide range of remotely sensed observations, while *Jasechko et al.* [2013] reported that *T* represents 80–90% of terrestrial *ET* based on the isotopic analysis of a global data set of large lakes and rivers. More recently, *Good et al.* [2015] estimated that the mean transpired fraction of *ET* is 64% based on satellite water vapor isotopic measurements and isotope mass budget. A model-based partitioning approach based on lateral ground flow also suggested that the *T* amounted to two thirds *ET* globally [*Maxwell and Condon*, 2016]. On the other hand, studies based on land surface models have suggested that the fraction of transpiration is much smaller, ranging around a mean value of about 43% [*Dirmeyer et al.,* 2006; *Lawrence et al.,* 2007, 2011; *Wang-Erlandsson et al.,* 2014; *Yoshimura et al.,* 2006], and some results based on satellite data yielded transpiration fractions as low as 24%. Finally, in the Coupled Model Intercomparison Project 5 (*CMIP5*), the fraction of *T* varies from 22% to 58%, with an ensemble mean of 43% (supporting information Figure S1). These uncertainties mostly arise from methodological assumptions that cannot be directly contrasted against field observations. While some studies have compared in situ site measurements with global model simulation results [*Schlesinger and Jasechko*, 2014; *Wang et al.,* 2014], the limited spatial scale of in situ studies—on the order of a few plants to several hectares—hampers the ability to upscale results to global mean values. The wide range of $T/(E + T + I)$ values in previous studies reflects how poorly we understand *ET* partitioning, with the corresponding implications for the terrestrial water and carbon cycles.

The relative contribution of transpiration to evapotranspiration has been found to be dependent on soil moisture availability [*Denmead and Shaw*, 1962; *Shuttleworth and Wallace*, 1985], climatic factors such as vapor pressure deficit [*Granier et al.,* 1996], and turbulent characteristics [*Tuzet et al.,* 1997]. Recently, the fraction of *T* has been directly linked to vegetation morphological attributes [*Wang et al.,* 2014; *Zhou et al.,* 2016], in particular, leaf area index (*LAI*, *Wang et al.* [2014]). Transpiration is directly related to canopy conductance, which is positively related to *LAI*; therefore, it is not surprising that *LAI* can act as a control over *ET* partitioning [*Good et al.,* 2014; *Schlesinger and Jasechko*, 2014; *Wang et al.,* 2014]. The advantage of exploiting the relationship between $T/(E+T+I)$ and *LAI* is that results can be easily extended to the global scales, since *LAI* data are available from polar satellites. However, the ratio $T/(E+T+I)$ varies greatly among ecosystem types because of interactions among plant morphology, environmental conditions, and stomatal regulation [*Raz-Yaseef et al.,* 2012]. Within an ecosystem, variations in weather conditions, growth stage, and soil moisture can result in large temporal variability in $T/(E+T+I)$. Moreover, the $T/(E+T+I)$ versus *LAI* relationship is robust only if the intercepted water is a small fraction of the total *ET*, given the parallel dependence of *I* on *LAI*. In other words, *LAI* is a good predictor for $T/(E+T)$ only; thus, to derive $T/(E+T+I)$ (i.e., *T*/*ET*), the magnitude of *I* needs to be known. Current understanding of the interception process suggests that *I* depends mainly on rainfall amount and intensity, aerodynamic conductance, canopy morphology, and *LAI* [*Miralles et al.,* 2010; *van Dijk et al.,* 2015]. Even though current interception estimates at global scales remain uncertain, several data sets of *I*, which are based on satellite observations, have been developed in recent years [*Miralles et al.,* 2016].

In summary, quantitative *ET* partitioning at the global scale is somewhat poor and not directly linked to the insights gained from site measurements. An improved estimate of the *ET* partitioning at the global scale and its geographic distributions should reduce uncertainties in modeling of the atmosphere-land water exchange, improve our ability to predict river runoffs, and help to inform management of water resources. Here, to quantify the fraction of *T* at the global scale, we develop a new *ET* partitioning algorithm that uses ecosystem-specific *LAI* regressions. We first develop regression equations between $T/(E+T)$ and *LAI* for six ecotypes to upscale site measurements from 64 previous studies and estimate $T/(E+T)$,and then apply *ET* and *I* estimate from remote sensing and land surface models to derive global $T/(E+T+I)$ ratios. Our results show that transpiration accounts for about 57.2% (uncertainty range of 42.9–74.9%) of the global terrestrial evapotranspiration.

2. Methods

We develop a new *ET* partitioning approach based on the estimated *ET*, *I*, fraction of each land cover class F_{v_i} (varying in the range of 0–1, where *i* is vegetation class), and *LAI* regression. The total transpiration *T* in each grid is calculated as

$$T = \sum_{i=1}^{n} (E+T) \times F_{v_i} \times aLAI^b \tag{1}$$

where *a* and *b* are two regression coefficients specific to land cover class *i*. There are a total of six vegetation classes in this calculation.

We establish the relationship between *LAI* and $T/(E+T)$ for each vegetation class using data found in the literature, as $T/(E+T) = aLAI^b$. The following screening criteria are used when selecting data from the published literature: (1) the ratio $T/(E+T)$ is reported either from direct site-based measurement of the component fluxes (*E* and *T*) or from isotopic tracer methods; (2) *LAI* is quantified during the measurement period; and (3) vegetation types are reported.

A total of 64 individual ground studies published before 30 September 2016 are included in our analysis. These studies are based on a range of measuring techniques, such as combination of eddy covariance systems, Bowen ratio systems, weighing lysimeters, sap flow meters, leaf conductance upscaling, chamber measurements, and isotopic measurements. The *E*, *T*, $E+T$ (or *ET-I*), and *LAI* values recorded directly in the tables or text in these original papers are summarized in supporting information Table S1. The observations are divided into six vegetation classes, including four upland natural vegetation classes [broad-leaf forests, needle-leaf forests, mixed forests (a combination of broad-leaf and needle-leaf trees), and shrubs-grasses],

a wetland class, and a cropland class. The grouping of upland natural ecosystems is based on permanence of aboveground biomass, canopy phenology, and leaf type, which are the key factors in determining stomatal conductance. Wetlands and crops are treated separately from the other vegetation classes due to their different root-zone water and nutrient availability. Tundra ecosystems are included in the shrub-grass class because of lack of field observations to constrain the *E/ET* versus *LAI* relationship as an independent tundra class. To reduce random error, the data obtained in cropland class are averaged into 0.5-*LAI* bins because this class is a mixture of different species, such as corn, wheat, rice, cowpeas, grapes, lupin, coffee, and sunflower. For the other five vegetation classes, the number of data samples is too small to perform bin averaging. A regression procedure is applied to equation (1) against a subset of the data for each class to find the best-fit coefficients *a* and *b* for that class.

There is no consensus as to which global *ET* product is most accurate [*Miralles et al.,* 2016*; McCabe et al.,* 2016]. Although some simulations have produced similar results, they are not always based on independent sources and therefore may share common biases related to the use of a common calibration or forcing data set and to common model assumptions [*Mueller et al.,* 2013]. To avoid these problems, three independent *ET* products are used. (1) *ET* estimated by the Community Land Model 4.5 SP (*CLM*, *Oleson et al.* [2013]): This is a physically based model at a 1° resolution. The model divides a grid cell into dry foliage, wet foliage (due to interception), and exposed soil. The dry foliage is further divided into sunlit and shaded portions. Computation of water vapor flux is made for each of these pathways. (2) Remote sensing-based *ET* product called *GLEAM* (Global Land Surface Evaporation: The Amsterdam Model, see *Miralles et al.* [2011] and *Martens et al.* [2016]). *GLEAM* is designed to maximize the use of satellite-based observations to create a spatially coherent estimate of the evaporative flux *ET* over land at daily and 0.25° resolutions. The method relies on a Priestley and Taylor approach to derive daily potential evaporation estimates from observed surface net radiation and surface air temperature, which are then constrained based on of soil moisture and vegetation water content observations. The potential evaporation is adjusted downward on the basis of soil moisture and phenology observations to obtain the actual *ET*. (3) *ET* estimated from Penman-Monteith-Leuning (*PML*) model [*Zhang et al.,* 2016]: *PML* is a simple biophysical model based on remote sensing *LAI* and separate versions of the Penman-Monteith equation for soil evaporation and plant transpiration. In *PML*, monthly *ET* estimates come from the aggregation of their individual components at each 0.5° grid cell. Generally, global patterns of annual mean *ET* estimated from these three products reveal a high correspondence (supporting information Figure S2).

Likewise, three different *I* products are adopted in this study. The first *I* product comes from the *CLM* and is derived through a simple model based on the observed precipitation, *LAI*, and stem area index (*SAI*). The second *I* product is obtained from *GLEAM*, which uses Gash's analytical model based on observed precipitation and vegetation fractional cover [*Miralles et al.,* 2010]. The third *I* product comes from *PML* and is also calculated from a modified version of Gash's rainfall interception model. Different from *ET* products, a significantly higher global mean $I/(E+T+I)$ value of 20% is found for *CLM*, compared to 11% and 10% of *GLEAM* and *PML*, respectively (supporting information Figure S3).

Finally, we use *LAI* data derived from four remotely sensed data sets: *GIMMS3g* [*Guay et al*., 2015], Improved *LAI* [*Yuan et al.,* 2011], *GLASS* [*Xiao et al.,* 2014], and *GLOMAPLAI*. The 1° resolution International Geosphere Biosphere Program (*IGBP*) land cover data set [*Friedl et al.,* 2010], which is based on the Land Cover Type Climate Modeling Grid (*MCD12C1*) created by Terra and Aqua Moderate Resolution Imaging Spectroradiometer observations made in 2001, is also used to classify past in situ studies and derive the *a* and *b* parameters (see equation (1)) for the fraction of each land cover class (F_v) per pixel. The 17 *IGBP* land cover classes are reclassified into six land cover classes, to match the global synthesis of the *LAI* control on the *ET* partitioning analysis (supporting information Table S2).

All data products are regridded and averaged into a 1° resolution and monthly timescale. In each grid, *T* is calculated by equation (1) in monthly timescale from 1982 to 2014 (if data are available). There are a total of 36 combinations of *LAI*, *ET*, and *I* products, corresponding to 36 permutations of *T*. Combining these permutations with the three *ET* products yield a total of 108 ensemble members for $T/(E+T+I)$ (see flow diagram in supporting information Figure S4). The monthly *T* and *ET* are then averaged into annual mean to calculate annual $T/(E+T+I)$. The area and *ET* weighted ensemble mean ratios of global $T/(E+T+I)$ are computed from the 108 ensemble members and are averaged over annual time steps. Our upscaling methodology

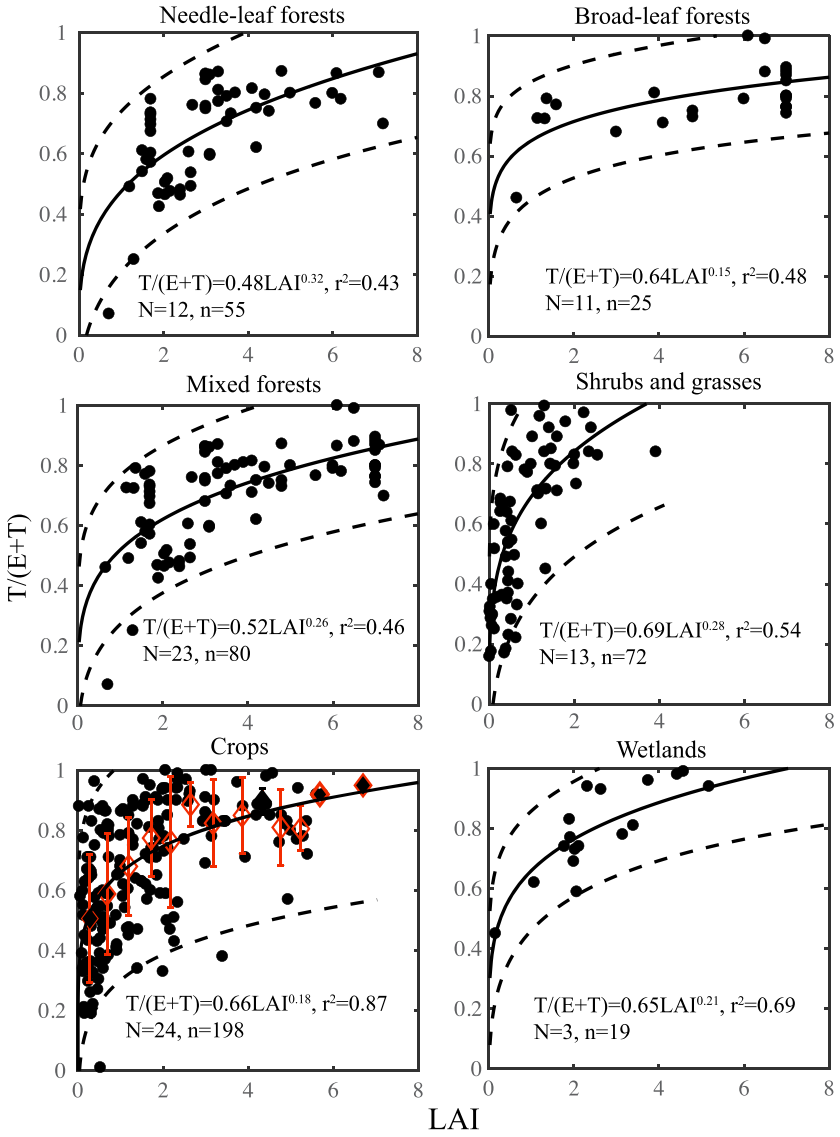

Figure 1. Ecosystem relationships between *LAI* and $T/(E+T)$. Black points are obtained from previous studies. Red open diamonds with error bars in crops class are 0.5-bin *LAI* averaged of black points and the standard deviation. Solid line is a regression of the individual data points (except for the crop class, which is estimated from the bin averages). *N* is the number of studies, and *n* is available data points in each class. Dash lines are 95% confidence bounds.

omits variations caused by daily to seasonal variations in soil moisture, groundwater availability, and vapor pressure deficit but considers interannual climate variability implicitly because the *ET* and *LAI* products vary interannually.

3. Results

The site-level data indicate that *LAI* is a good predictor of $T/(E+T)$ (Figure 1). Overall, the strong correlation between *LAI* and $T/(E+T)$ obtained from the different data sets suggests that *LAI* can be considered the first-order factor affecting *ET* partitioning. The variability of $T/(E+T)$ can result from biotic and abiotic responses to weather and soil moisture dynamics at daily to weekly scales. However, at the seasonal timescale, such variability becomes small, and the ratio converges toward a stable mean state, which is set by *LAI* [*Berkelhammer et al.,* 2016]. The $T/(E+T)$ curves bear remarkable resemblance to the seasonal pattern predicted by a two-source *ET* modeling [*Hu et al.,* 2008; *Shuttleworth and Wallace*, 1985].

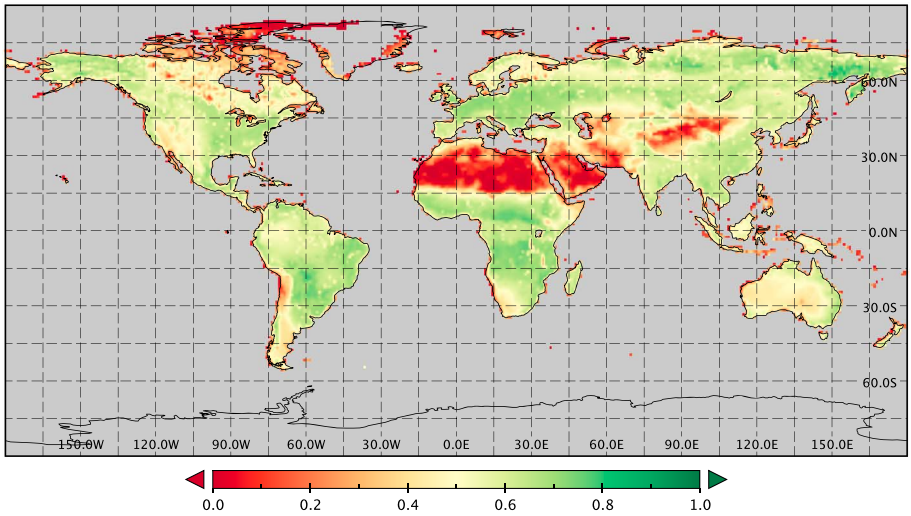

Figure 2. The ensemble means of $T/(E+T+I)$ ratio using different data sources for *ET*, *I*, and *LAI*, with a total of 108 different data source permutations.

The *LAI* regression varies substantially among the different vegetation classes (Figure 1 and supporting information Table S3). For shrubs and grasses, $T/(E+T)$ can be high even under low *LAI* conditions (e.g., $T/(E+T)=0.69$ at $LAI=1$, based on the regression equation), and at larger values of *LAI*, it dramatically increases (e.g., $T/(E+T)=0.93$ for $LAI=3$). This agrees with the results from catchment and site-scale isotopic analyses of vegetated areas dominating by sparse grass vegetation in the western United States, showing that $T/(E+T)$ is higher than 70% [*Schlesinger and Jasechko,* 2014]. Likewise, crops may also have high $T/(E+T)$ under low *LAI* conditions ($T/(E+T)=0.66$, $LAI=1$), potentially influenced by a high water use efficiency and the fact that agricultural plants are typically less constrained by environmental stresses [*Wang et al.,* 2014]. On the other hand, forests tend to have lower $T/(E+T)$ ratios at low *LAI* values (e.g., $T/(E+T)=0.48$ for needle-leaf forests and $T/(E+T)=0.64$ for broad-leaf forests, both for $LAI=1$). This is arguably due to the shading effect of grasses and shrubs causing lower fractions of exposed bare soil and lower stomatal conductance of trees [*Hetherington and Woodward*, 2003; *Teuling et al.,* 2010; *Wang et al.,* 2013].

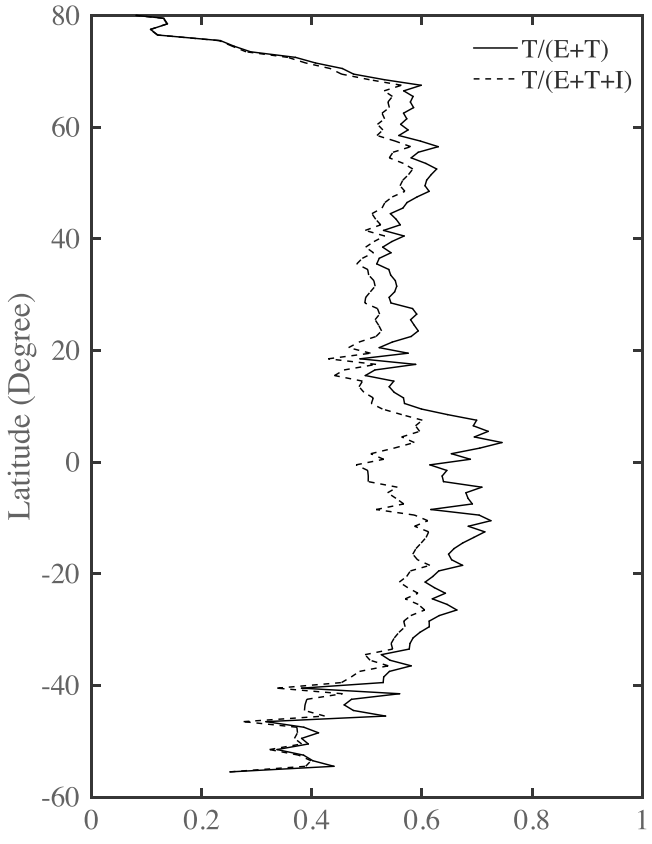

Figure 3. The zonally averaged ensemble means $T/(E+T+I)$ and $T/(E+T)$.

The globally averaged $T/(E+T+I)$ ratio is 57.2% (with standard deviation ± 6.8%) based on a total of 108 different data source permutations or ensemble members. No significant trend in $T/(E+T+I)$ is detected from 1982 to 2014

Table 1. Comparison of $T/(E+T+I)$ (%) for Several Vegetation Types Among Different Studies

Vegetation Class	*Zhou et al.* [2016]	*Wang-Erlandsson et al.* [2014]	*Miralles et al.* [2011]	*Schlesinger and Jasechko* [2014]	This Study
Crops	62–69	72	92		66
Shrubs and grasses	60	58–70	72–90	47–62	65
Needle leave forests	56	50–52	70	55–65	55
Broad leave forests	52	54–64	79	70	61
Mixed forests		57			55
Wetlands		31–37			31

(supporting information Figure S5), although a slight increase ($0.068 \pm 0.045\ m^2\ m^{-2}\ yr^{-1}$) of *LAI* over 25% to 50% of the global vegetated area was reported [*Zhu et al.,* 2016]. For comparison, the *CMIP5* modeling results and remote sensing *ET* products reveal no significant trend in $T/(E+T+I)$ (supporting information Figure S6 and Figure S7). The 30 year mean of global $T/(E+T+I)$ varies from 42.9% to 74.9% among ensemble members (supporting information Table S4 and Figure S5). The fraction of *T* uncertainty is small among the three adopted *ET* products ($T/(E+T+I)$ is $55.1 \pm 6.7\%$, $55.2 \pm 6.8\%$, $61.3 \pm 6.8\%$ if *ET* is derived from *GLEAM*, *CLM*, and *PML*, respectively). One of the main uncertainties stems from variations among the interception data products: $T/(E+T+I)$ is $52.2 \pm 7.0\%$ if *I* is derived from *CLM* and increases to $60.0 \pm 6.7\%$ and $59.2 \pm 6.8\%$ if *I* is derived from *GLEAM* and *PML*, respectively. Another uncertainty is related to the *LAI* data sets. $T/(E+T+I)$ is $63.0 \pm 6.9\%$ if *LAI* is derived from *GIMMS3g* and decreases to $57.3 \pm 7.0\%$, $55.9 \pm 6.4\%$, and $52.0 \pm 6.8\%$ if *LAI* is derived from *GLASS*, Improved *LAI*, and *GLOMAPLAI*, respectively.

Figure 2 shows the global distribution of the ensemble means of $T/(E+T+I)$. Except for deserts and glaciers, *T* is the dominant component of the annual *ET*. The highest $T/(E+T+I)$ is found in central Africa covered by grass and shrub. On the other hand, the highest $T/(E+T)$ is found in the Amazon rainforests, because of large *LAI* (responsible for both *T* and *I*) in this region (supporting information Figure S8). The zonally averaged $T/(E+T+I)$ varies from 1% to 61%, and $T/(E+T)$ varies from 1% to 75%, exhibiting distinct latitudinal patterns, changing as a function of vegetation density and decreasing toward the poles (Figure 3). Low $T/(E+T+I)$ and $T/(E+T)$ ratios are found near the poles (latitudes north of 60°N and south of 40°S). Between 10°N and 20°S, $T/(E+T+I)$ fluctuates around 55% while $T/(E+T)$ around 68%. $T/(E+T)$ is much higher than $T/(E+T+I)$ in this zone than in midlatitudes because a larger fraction of *ET* is contributed by evaporation of intercepted water.

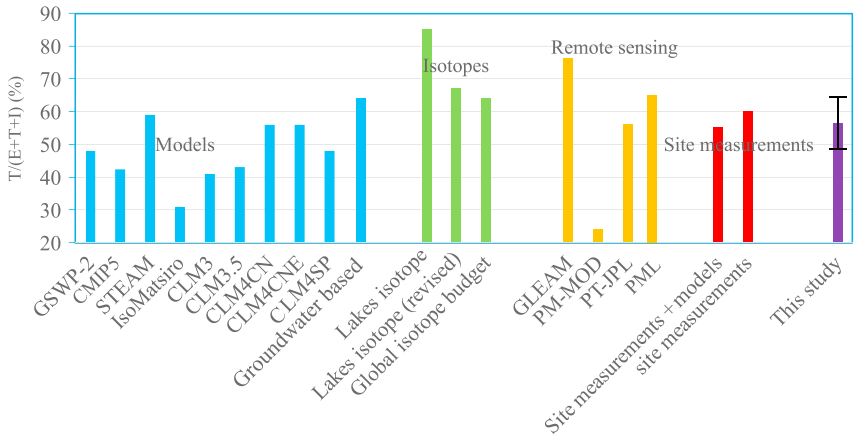

Figure 4. Comparison of $T/(E+T+I)$ estimated by different methods. Methods include *GSWP-2* [*Dirmeyer et al.,* 2006], *CMIP5* (corresponding to the ensemble mean of 21 models in *CMIP5*, see supporting information Figure S1), *STEAM* [*Wang-Erlandsson et al.,* 2014], *IsoMatsiro* [*Yoshimura et al.,* 2006], *CLM3* [*Lawrence et al.,* 2007], *CLM3.5*, *CLM4CN*, *CLM4CNE*, *CLM4SP* [*Lawrence et al.,* 2011], lake isotope [*Jasechko et al.,* 2013], lake isotope (revised) [*Coenders-Gerrits et al.,* 2014], global isotope budget [*Good et al.,* 2015], groundwater-based partitioning [*Maxwell and Condon*, 2016], *GLEAM* [*Miralles et al.,* 2016], *PM-MOD* [*Miralles et al.,* 2016], *PT-JPL*[*Miralles et al.,* 2016], *PML* [*Zhang et al.,* 2016], site measurements + models [*Schlesinger and Jasechko*, 2014], and site measurements [*Wang et al.,* 2014]. The error bar represents the standard deviation (±6.8%) in this study.

The estimated annual $T/(E+T+I)$, classified by vegetation types, is further compared to the values reported in previous studies (Table 1). Overall, *T* is the dominant component in total *ET* for all vegetation classes, with the $T/(E+T+I)$ ratio ranging from 55% to 66%, except wetlands which have a lower ratio of 33% because of low *LAI*. Our estimated annual $T/(E+T+I)$ based on vegetation classification is fairly similar to the *ET* partitioning results based on the concept of water use efficiency [*Zhou et al.,* 2016] and land surface model *STEAM* [*Wang-Erlandsson et al.,* 2014], but is lower than the values reported by in *Jasechko et al.* [2013] likely due in part to the citation of an interception value that is substantially lower than more recent interception estimates used here (see [*Schlesinger and Jasechko*, 2014]. The crop class has the highest $T/(E+T+I)$ among the ecosystem types considered, in agreement with the high $T/(E+T)$ from the *LAI* regressions.

Figure 4 provides a summary of the *ET* partitioning values reported in the literature and how they compare with our result. Our global $T/(E+T+I)$ estimate ranges from 42.9% to 74.9% among the individual ensemble members. The ensemble mean ratio of $57.2 \pm 6.8\%$ is about 5–10% lower than a recently reported isotopically based partitioning estimate [*Good et al.,* 2015], from site scales estimates [*Schlesinger and Jasechko*, 2014; *Wang et al.,* 2014] and from a model that accounts for groundwater flow [*Maxwell and Condon*, 2016], but 10% higher than the ensemble mean of the global climate model results posted in the *CMIP5* data depository (supporting information Figure S1).

4. Discussion

In our study, the 17 land cover types in the *IGBP* are reclassified into six land cover classes, in order to produce robust regression. This regrouping can introduce uncertainties in the estimated $T/(E+T)$ (Methods and supporting information Table S2). For example, crops display large variations in $T/(E+T)$ under similar *LAI* conditions because they are mixtures of different species, such as corn, wheat, rice, cowpeas, grapes, lupin, coffee, and sunflower (supporting information Table S1), although an acceptable correlation is obtained after bin averaging with an *LAI* increment of 0.5. We tried dividing the crops into C_3 and C_4 groups, but the correlation in the *LAI* regression did not improve. Perhaps as more site-level data become available in the published literature, subclassification according to stomatal characteristics may strengthen the regression analysis. Because shrubs and grasses have different *LAI* dynamics and different rooting depth, the further subclassification may also be required to break this group into two classes.

Two ecosystem classes require further improvement. First, in savanna ecosystems, overstory (trees) and understory (grass) coexist, and their transpiration contributions to *ET* should be considered separately, due to their different water uptake processes. Unfortunately, current land cover and *LAI* data sets do not make a distinction between overstory and understory vegetation. This might be a reason for the large discrepancies of modeled *ET* and *T* in savanna regions in previous *LSM* applications [e.g., *Miralles et al.,* 2016]. Second, in tundra ecosystems, evaporation from moss and lichens is the main component of *ET*. However, the scarcity of field measurements does not allow us to establish the relationship between *LAI* and $T/(E+T)$ for this ecosystem class.

Site-level measurement errors can also introduce uncertainties to the *LAI* regression. In some studies, transpiration from understory vegetation was not well constrained, with many studies suggesting understory vegetation contributes 10% to 50% of the total *ET* and this contribution tends to increase with decreasing *LAI* [*Kelliher et al.,* 1997; *Wilson et al.,* 2000]. Thus, the *LAI* regression may lead to overestimation of sap flow based on those publications that determined *E* using lysimeter or chamber methods and *ET* using eddy covariance. Both isotopic and nonisotopic measurements are included in our *LAI* regression estimation. Most isotope-based studies have shown that *T* generally contributes more than 70% to the *ET*, while nonisotopic measurements generally lead to smaller *T* fractions [*Schlesinger and Jasechko*, 2014; *Sutanto et al.,* 2014]. Several possible explanations for this discrepancy have been offered [*Schlesinger and Jasechko*, 2014; *Sutanto et al.,* 2014], although some comparative studies found no systematic difference between isotope and nonisotope methods [*Wang et al.,* 2015; *Wen et al.,* 2016].

It is possible that the discrepancy between stand-scale-isotope and nonisotope approaches may result from a mismatch at the temporal scale. The stand-scale isotope-based method is robust under conditions of high water vapor flux. Under weak turbulence conditions (e.g., in the morning or evening) when water vapor flux is small, the uncertainties with isotopic estimations are quite large [*Wei et al.,* 2015]. Thus, the isotope method is usually restricted to estimating *T*/*ET* for the midday hours of high *T* [*Wang et al.,* 2013]. On the other hand,

nonisotope methods are used in all time periods, including nighttime when *T* is weak but *E* still occurs. Thus, the isotopic measurements included in the *LAI* regression estimation may result in an overestimation of the fraction of *T*.

To explore the uncertainties resulting from the *LAI* regression procedure, we conducted a Monte Carlo analysis using 1000 realizations and assuming a Gaussian error distribution for the regression coefficients *a* and *b*, for all of 108 combinations. The results show an averaged value of 56.0 ± 7.7% for the fraction of *T*, which is close to our ensemble mean. Therefore, uncertainties resulting from the *LAI* regression estimation can be omitted for the global *ET* partitioning.

A large potential bias error in *ET* partitioning stems from *I*. Among the three interception data products, the ratio $I/(E+T+I)$ varies from 10% to 20%. Only limited direct observations of canopy interception loss have been reported in the $T/(E+T+I)$ studies for various regions of the globe [*Barbour et al.,* 2005; *Wilson et al.,* 2000]. We analyzed the data from five long-term *ET* partitioning studies that measured at least two of the three components of the *ET* flux and compared the results with the global *I* data sets we used. We find that $I/(E+T+I)$ generally remains some uncertainties in all the *I* data sets we used (supporting information Table S5). Compared to the work on rainfall interception, there have been fewer studies on evaporation of intercepted snow [*Miralles et al.,* 2016]. The model community is yet to develop robust snow interception/evaporation models [*Miralles et al.,* 2010, 2016]. Resolving terrestrial interception remains critical to constraining evapotranspiration partitioning estimates. For example, two isotope-based global *ET* partitioning studies calculate similar $T/(E+T)$ values (>90% [*Good et al.,* 2015; *Jasechko et al.,* 2013]) but present different $T/(E+T+I)$ values (85 ± 5% and 64 ± 13%) because they report different interception fluxes. Better constraining global land interception can improve $T/(E+T+I)$ estimates.

Although four *LAI* products based on the *AVHRR* and *MODIS* satellites have been extensively validated by field measurements, the spatial distributions, magnitudes, and temporal variations of *LAI* are somewhat different. For example, the *GLASS LAI* data show statistically significant increasing trend of over 50% of vegetated lands from the 1982 to 2009 period, while *GIMMS3g* data show a smaller trend value of 25% [*Zhu et al.,* 2016]. These discrepancies are not only caused by using different methodologies, different strategies, and different *AVHRR* products in each *LAI* products but also raised from lacking of onboard calibration and orbital loss problem of *AVHRR* sensors [*Tucker et al.,* 2005; *Zhu et al.,* 2016]. Further improvement of remote sensing *LAI* products at high spatial and temporal resolutions will enable us to extrapolate the *LAI* regression to obtain spatially explicit estimates of $T/(E+T+I)$ across the globe and its temporal variability. Nevertheless, the regression between $T/(E+T)$ and *LAI* suggests that vegetation density controls *ET* partitioning, and this control pattern varies among vegetation classes.

Vegetation feedback is largely uncertain in global climate models in terms of future predictions. Currently, most of the global climate models produce too small $T/(E+T+I)$. The mean $T/(E+T+I)$ for the 30 models considered is 43% (Figure 4), which is more than 10% lower than the current result. The current approach provides a new constraint that can help modelers to reduce the uncertainty of vegetation control on the global water cycle.

5. Conclusion

This study develops a new *ET* partitioning approach, through the combination of remote sensing, land surface model, and *LAI* regression obtained from 64 in situ measurements. The $T/(E+T)$ is well represented as a function of *LAI*. The *ET* estimated from *GLEAM*, *CLM*, and *PML* showed similar large-scale patterns, while *I* estimated from *CLM* is significantly higher than that derived from *PML* and *GLEAM*. Based on global synthesis of *LAI* control on *ET* partitioning and different *ET* products, the $T/(E+T+I)$ ratio varies from 42.9% to 74.9% among the 108 ensemble members considered, with an ensemble mean of 57.2 ± 6.8% at the global scale. Further study on the role of interception is required because uncertainty in canopy interception loss estimation is the largest source of bias in *ET* partitioning.

Acknowledgments
The authors would like to thank Xiaogang He, Natsuki Yoshida, Yusuke Satoh, and Hyungjun Kim for sharing their data. This study is supported by the Japanese Society for the Promotion of Science (grants 26289160 and 23226012), the SOUSEI Program and the ArCS project of MEXT, Project S-12 from the Japanese Ministry of Environment, the CREST Program of the Japanese Science and Technology Agency, and the U.S. National Science Foundation (grant AGS-1520684). All the data used in this study are available on request from the corresponding author (zhongwang.wei@yale.edu).

References

Barbour, M. M., J. E. Hunt, A. S. Walcroft, G. N. D. Rogers, T. M. McSeveny, and D. Whitehead (2005), Components of ecosystem evaporation in a temperate coniferous rainforest, with canopy transpiration scaled using sapwood density, *New Phytol.*, *165*(2), 549–558.

Berkelhammer, M., D. C. Noone, T. E. Wong, S. P. Burns, J. F. Knowles, A. Kaushik, P. D. Blanken, and M. W. Williams (2016), Convergent approaches to determine an ecosystem's transpiration fraction, *Global Biogeochem. Cycles*, *30*, 933–951, doi:10.1002/2016GB005392.
Coenders-Gerrits, A. M. J., R. J. van der Ent, T. A. Bogaard, L. Wang-Erlandsson, M. Hrachowitz, and H. H. G. Savenije (2014), Uncertainties in transpiration estimates, *Nature*, *506*(7487), E1–E2.
Denmead, O. T., and R. H. Shaw (1962), Availability of soil water to plants as affected by soil moisture content and meteorological conditions, *Agron. J.*, *54*, 385–390.
Dirmeyer, P. A., X. Gao, M. Zhao, Z. Guo, T. Oki, and N. Hanasaki (2006), GSWP-2: Multimodel analysis and implications for our perception of the land surface, *Bull. Am. Meteorol. Soc.*, *87*(10), 1381–1397.
Friedl, M. A., D. Sulla-Menashe, B. Tan, A. Schneider, N. Ramankutty, A. Sibley, and X. Huang (2010), MODIS Collection 5 global land cover: Algorithm refinements and characterization of new datasets, *Remote Sens. Environ.*, *114*(1), 168–182.
Good, S. P., K. Soderberg, K. Guan, E. G. King, T. M. Scanlon, and K. K. Caylor (2014), δ^2H isotopic flux partitioning of evapotranspiration over a grass field following a water pulse and subsequent dry down, *Water Resour. Res.*, *50*, 1410–1432, doi:10.1002/2013WR014333.
Good, S. P., D. Noone, and G. Bowen (2015), Hydrologic connectivity constrains partitioning of global terrestrial water fluxes, *Science*, *349*(6244), 175–177.
Granier, A., R. Huc, and S. T. Barigah (1996), Transpiration of natural rain forest and its dependence on climatic factors, *Agric. For. Meteorol.*, *78*(1–2), 19–29.
Guay, K. C., P. S. A. Beck, and, S. J. Goetz (2015), Long-Term Arctic Growing Season NDVI Trends from GIMMS 3g, 1982–2012, Data set. [Available at http://daac.ornl.gov] from Oak Ridge National Laboratory Distributed Active Archive Center, Oak Ridge, Tenn.
Hetherington, A. M., and F. I. Woodward (2003), The role of stomata in sensing and driving environmental change, *Nature*, *424*(6951), 901–908.
Hu, Z. M., G. R. Yu, Y. L. Fu, X. M. Sun, Y. N. Li, P. L. Shi, Y. F. Wangw, and Z. M. Zheng (2008), Effects of vegetation control on ecosystem water use efficiency within and among four grassland ecosystems in China, *Global Change Biol.*, *14*(7), 1609–1619.
Jasechko, S., Z. D. Sharp, J. J. Gibson, S. J. Birks, Y. Yi, and P. J. Fawcett (2013), Terrestrial water fluxes dominated by transpiration, *Nature*, *496*(7445), 347–350.
Kelliher, F. M., et al. (1997), Evaporation from an eastern Siberian larch forest, *Agric. For. Meteorol.*, *85*(3–4), 135–147.
Lawrence, D. M., P. E. Thornton, K. W. Oleson, and G. B. Bonan (2007), The partitioning of evapotranspiration into transpiration, soil evaporation, and canopy evaporation in a GCM: Impacts on land–atmosphere interaction, *J. Hydrometeorol.*, *8*(4), 862–880.
Lawrence, D. M., et al. (2011), Parameterization improvements and functional and structural advances in version 4 of the Community Land Model, *J. Adv. Model Earth Syst.*, *3*, M03001, doi:10.1029/2011MS00045.
Martens, B., D. G. Miralles, H. Lievens, R. van der Schalie, R. A. M. De Jeu, D. Fernández-Prieto, H. E. Beck, W. A. Dorigo, and N. E. Verhoest (2016), GLEAM v3: Satellite-based land evaporation and root-zone soil moisture, *Geosci. Model Dev. Discuss.*, doi:10.5194/gmd-2016-162.
Maxwell, R. M., and L. E. Condon (2016), Connections between groundwater flow and transpiration partitioning, *Science*, *353*(6297), 377–380.
Mccabe, M. F., A. Ershadi, C. Jiménez, D. G. Miralles, D. Michel, and E. F. Wood (2016), The GEWEX LandFlux Project: Evaluation of model evaporation using tower-based and globally gridded forcing data, *Geosci. Model Dev.*, *9*(1), 283–305.
Miralles, D. G., J. H. Gash, T. R. H. Holmes, R. A. M. de Jeu, and A. J. Dolman (2010), Global canopy interception from satellite observations, *J. Geophys. Res.*, *115*, D16122, doi:10.1029/2009JD013530.
Miralles, D. G., R. A. M. De Jeu, J. H. Gash, T. R. H. Holmes, and A. J. Dolman (2011), Magnitude and variability of land evaporation and its components at the global scale, *Hydrol. Earth Syst. Sci.*, *15*(3), 967–981.
Miralles, D. G., et al. (2016), The WACMOS-ET project—Part 2: Evaluation of global terrestrial evaporation data sets, *Hydrol. Earth Syst. Sci.*, *20*(2), 823–842.
Mueller, B., et al. (2013), Benchmark products for land evapotranspiration: LandFlux-EVAL multi-data set synthesis, *Hydrol. Earth Syst. Sci.*, *17*(10), 3707–3720.
Oleson, K., D. Lawrence, G. Bonan, B. Drewniak, M. Huang, C. Koven, S. Levis, F. Li, W. Riley, and Z. Subin (2013), Technical description of version 4.5 of the Community Land Model (CLM), NCAR Tech Rep., Note NCAR/TN-503+ STR, 422 pp., Natl. Cent. for Atmos. Res., Boulder, Colo., doi:10.5065/D6RR1W7M.
Raz-Yaseef, N., D. Yakir, G. Schiller, and S. Cohen (2012), Dynamics of evapotranspiration partitioning in a semi-arid forest as affected by temporal rainfall patterns, *Agric. For. Meteorol.*, *157*, 77–85.
Schlesinger, W. H., and S. Jasechko (2014), Transpiration in the global water cycle, *Agric. For. Meteorol.*, *189–190*, 115–117.
Shuttleworth, W. J., and J. S. Wallace (1985), Evaporation from sparse crops—an energy combination theory, *Q. J. R. Meteorol. Soc.*, *111*(469), 839–855.
Sutanto, S. J., B. van den Hurk, P. A. Dirmeyer, S. I. Seneviratne, T. Röckmann, K. E. Trenberth, E. M. Blyth, J. Wenninger, and G. Hoffmann (2014), HESS Opinions "A perspective on isotope versus non-isotope approaches to determine the contribution of transpiration to total evaporation", *Hydrol. Earth Syst. Sci.*, *18*(8), 2815–2827.
Teuling, A. J., et al. (2010), Contrasting response of European forest and grassland energy exchange to heatwaves, *Nat. Geosci.*, *3*(10), 722–727.
Tucker, C. J., J. E. Pinzon, M. E. Brown, D. A. Slayback, E. W. Pak, R. Mahoney, E. F. Vermote, and N. El Saleous (2005), An extended AVHRR 8-km NDVI dataset compatible with modis and spot vegetation NDVI data, *Int. J. Remote Sens.*, *26*, 4485–4498.
Tuzet, A., J. F. Castell, A. Perrier, and O. Zurfluh (1997), Flux heterogeneity and evapotranspiration partitioning in a sparse canopy: The fallow savanna, *J. Hydrol.*, *188–189*, 482–493.
van Dijk, A. I. J. M., et al. (2015), Rainfall interception and the coupled surface water and energy balance, *Agric. For. Meteorol.*, *214–215*, 402–415.
Wang, L., S. Niu, S. P. Good, K. Soderberg, M. F. McCabe, R. A. Sherry, Y. Luo, X. Zhou, J. Xia, and K. K. Caylor (2013), The effect of warming on grassland evapotranspiration partitioning using laser-based isotope monitoring techniques, *Geochim. Cosmochim. Acta*, *111*, 28–38.
Wang, L., S. P. Good, and K. K. Caylor (2014), Global synthesis of vegetation control on evapotranspiration partitioning, *Geophys. Res. Lett.*, *41*, 6753–6757, doi:10.1002/2014GL061439.
Wang, P., T. Yamanaka, X.-Y. Li, and Z. Wei (2015), Partitioning evapotranspiration in a temperate grassland ecosystem: Numerical modeling with isotopic tracers, *Agric. For. Meteorol.*, *208*, 16–31.
Wang-Erlandsson, L., R. J. van der Ent, L. J. Gordon, and H. H. G. Savenije (2014), Contrasting roles of interception and transpiration in the hydrological cycle—Part 1: Temporal characteristics over land, *Earth Syst. Dyn.*, *5*(2), 441–469.
Wei, Z., K. Yoshimura, A. Okazaki, W. Kim, Z. Liu, and M. Yokoi (2015), Partitioning of evapotranspiration using high-frequency water vapor isotopic measurement over a rice paddy field, *Water Resour. Res.*, *51*, 3716–3729, doi:10.1002/2014WR016737.

Wen, X., B. Yang, X. Sun, and X. Lee (2016), Evapotranspiration partitioning through in-situ oxygen isotope measurements in an oasis cropland, *Agric. For. Meteorol.*, *230–231*, 89–96.
Wilson, K. B., P. J. Hanson, and D. D. Baldocchi (2000), Factors controlling evaporation and energy partitioning beneath a deciduous forest over an annual cycle, *Agric. For. Meteorol.*, *102*(2–3), 83–103.
Xiao, Z., S. Liang, J. Wang, P. Chen, X. Yin, L. Zhang, and J. Song (2014), Use of general regression neural networks for generating the GLASS leaf area index product from time-series MODIS surface reflectance, *IEEE Trans. Geosci. Remote Sens.*, *52*(1), 209–223.
Yoshimura, K., S. Miyazaki, S. Kanae, and T. Oki (2006), Iso-MATSIRO, a land surface model that incorporates stable water isotopes, *Global Planet. Change*, *51*(1–2), 90–107.
Yuan, H., Y. Dai, Z. Xiao, D. Ji, and W. Shangguan (2011), Reprocessing the MODIS Leaf Area Index products for land surface and climate modelling, *Remote Sens. Environ.*, *115*(5), 1171–1187.
Zhang, Y., et al. (2016), Multi-decadal trends in global terrestrial evapotranspiration and its components, *Sci. Rep.*, *6*, 19124, doi:10.1038/srep19124.
Zhou, S., B. F. Yu, Y. Zhang, Y. F. Huang, and G. Q. Wang (2016), Partitioning evapotranspiration based on the concept of underlying water use efficiency, *Water Resour. Res.*, *52*, 1160–1175, doi:10.1002/2015WR017766.
Zhu, Z., et al. (2016), Greening of the Earth and its drivers, *Nat. Clim. Change*, *6*, 791–795.